# A novel approach to model the transient behavior of solid-oxide fuel cell stacks

Vikram Menon [a], Vinod M. Janardhanan [b], Steffen Tischer [a], Olaf Deutschmann [a],*

[a] Institute for Chemical Technology and Polymer Chemistry, Karlsruhe Institute of Technology (KIT), Engesserstr. 20, 76131 Karlsruhe, Germany
[b] Department of Chemical Engineering, IIT Hyderabad, Yeddumailaram, Andhra Pradesh 502 205, India

## HIGHLIGHTS

► Novel approach to model solid-oxide fuel cell (SOFC) stacks in two and three dimensions.
► Hierarchical model developed.
► Results presented for a stack operated on pre-reformed hydrocarbon fuel.
► Transient response to load changes studied.

## ARTICLE INFO

## ABSTRACT

This paper presents a novel approach to model the transient behavior of solid-oxide fuel cell (SOFC) stacks in two and three dimensions. A hierarchical model is developed by decoupling the temperature of the solid phase from the fluid phase. The solution of the temperature field is considered as an elliptic problem, while each channel within the stack is modeled as a marching problem. This paper presents the numerical model and cluster algorithm for coupling between the solid phase and fluid phase. For demonstration purposes, results are presented for a stack operated on pre-reformed hydrocarbon fuel. Transient response to load changes is studied by introducing step changes in cell potential and current. Furthermore, the effect of boundary conditions and stack materials on response time and internal temperature distribution is investigated.

## 1. Introduction

Solid-oxide fuel cells (SOFCs) have been proposed as a power source for distributed or stationary power plants and mobile applications. This wide usability is due to their modularity, high electrical efficiency, low environmental pollution, fuel flexibility, and tolerance to fuel pollutants. A typical unit cell in a planar SOFC stack is composed of a positive electrode–electrolyte-negative electrode (PEN) assembly, interconnected plates on both sides, and gas seals. In practical applications of SOFCs, multiple cells are assembled to form a stack and a serial connection in an electric loop to generate high voltage and power.

An attractive feature is the possibility of SOFC being combined with other power generation systems (e.g., gas turbines) to achieve high overall electrical power generation efficiency, due to their high working temperatures [1–9]. One such application domain that draws considerable interest from the automobile industry is the use of SOFCs for auxiliary power units (APUs) because of their high efficiency and low emissions. For SOFC-based APUs, it is not trivial to operate the cells on pure hydrogen. Instead, operating the cells on reformate fuels from gasoline or diesel will be more attractive because these fuels are available on-board and can be reformed before usage as fuel. Furthermore, the APUs are subjected to frequent load changes which cannot be pre-determined. The control strategy and the power electronics associated with these applications may be quite complex [10–20]. Understanding the response time of a system is particularly important because of the frequently fluctuating nature of demand for electrical power.

In this paper, we present the development of a new stack model and its solution algorithm. The model is demonstrated with a pragmatic fuel composition for APUs. A number of issues, such as (i) required power rating of the APU, (ii) start-up time, (iii) response

to load changes, (iv) control strategies, (v) fuel choice, (vi) fuel utilization, (vii) stack degradation, and (vii) stack volume, need to be considered when addressing the application of SOFC as APUs. However, this paper – as a first step – focuses only on the development of the numerical algorithm, stack simulation, and transient response to load changes.

There is a great deal of literature addressing the dynamics of load changes during SOFC operation. Most of these modeling studies are either done for single channels [21–24], single cells [25–29] or for stacks containing small number of cells [30–35]. Solving the electrochemical model equations requires fixing either the operating cell potential or the current. Li et al. have studied the dynamic response of the cell to changes in fuel flow rates [32]. Even though Achenbach and Li et al. simulated cross-flow cells, the time constant reported by Li et al. is in the order of hours and that reported by Achenbach is in the order of a few minutes. Achenbach [36,37] examined the transient cell voltage performance due to temperature changes and perturbations in current density. Furthermore, Li et al. also reported that the time constants for different parts of the cell to reach steady state are different. Though both of these studies are done for internal reforming, the fuel compositions used differ slightly from each other. Nevertheless, the time constant reported by Li et al. differs largely from that reported by Achenbach. Therefore, it must be assumed that the time constant for the cell processes depends largely on the model parameters used. Unfortunately, it is not possible to make a direct comparison as the literature does not provide a comprehensive list of material properties and electrochemical model parameters.

A Laplace domain model has been considered by Padullés et al. [38] for the dynamics of a SOFC plant. However, the model does not consider changes in the transport fields along the gas flow channels and inside the electrodes. The model contemplated by Jurado [39] is similar. The author studied fuel cell response characteristics, in terms of real and reactive power, to frequency step and voltage step transients, respectively. The time constant of the cell voltage approximated to 0.03–0.05 s, although the exact operating conditions of the cell could not be determined. Lu et al. [40] have observed that there can be differences in time constants between different transport fields. However, the time constants of a particular transport field may also vary with different operating conditions. Such a study has been presented by Murshed et al. [41], in which load changes in current at different temperatures are introduced and the differences in voltage transients were observed. For a step change in current, the time constant of the voltage transient in their study was about 10–20 s, depending on the operating temperature. It may be mentioned that the time constant of an output for a stack is typically higher than that for a single cell. In case of a step change in the flow rate of $H_2$ or $O_2$, the time constant of voltage is about 5–10 s. For a step up in current density, the time constant is about 110–120 s, while in the case of a step down, it is about 200 s. Iora et al. [42] have imposed a ramp load change of ±2000 A m$^{-2}$ over a period of 60 s to study the transients in voltage.

The latter three dynamic stack models (Lu et al. [40]; Murshed et al. [41]; Iora et al. [42]) are non-isothermal and yet the time constants in these studies are in seconds. A much larger time constant is observed in the study of Hall and Colclaser [43]. In this non-isothermal model, the time constant of the cell terminal voltage is about 800 s for a step change in current density of about 43%. A still higher value of time constant is reported by Lin and Hong [44]. In response to a step change in current from 0.5 to 0.3 A cm$^{-2}$, the time constant of the voltage transient for a single cell was found to be about 30 min. Kazempoor et al. [53] have investigated the dynamic characteristics of SOFC systems in order to develop relevant control strategies. They applied two control strategies, i.e., cell constant fuel

flow rate and constant fuel utilization, to conclude that the latter strategy had smaller relaxation times and temperature gradients, and was better suited to control an SOFC operation. Moreover, they also considered an additional strategy involving introduction of step changes in inlet flow temperature, which resulted in relaxation times that were two times higher.

In none of the dynamic models discussed previously, detailed dynamics of the diffusion processes inside the porous electrodes were considered. However, the transients are greatly affected by the mass transfer resistances inside the electrodes, as can be seen in the study of Qi et al. [26,27]. In their earlier work [26], the authors had focused on cell impedance and diffusion resistances inside the electrodes. The diffusion considered is one-dimensional and Taylor's expansion is applied to derive the flux in the form of a transfer function. Transients in voltage and current are observed in response to a step change in the resistive load of the system. The authors concluded that the slow response following the fast response is due to the diffusion limitation inside the porous layer. Their subsequent model [27] is non-isothermal, but the diffusion considered is still one-dimensional and the approximations in deriving the transfer function model remain the same as before. None of the studies presented above are validated with experimental data.

In the present analysis, we report the modeling of a 30 cell stack made up of co-flow configuration. The fuel composition employed is 31.81% $H_2$, 36.56% $N_2$, 13.19% CO, 13.19% $CH_4$, 2.23% $CO_2$, and 3.02% $H_2O$. This fuel composition essentially results from mixing 3% $H_2O$ to the fuel from the partial oxidation of methane with air [45].

## 2. Modeling approach

### 2.1. Single unit cell

A quasi-two-dimensional model reported previously is used for the simulation of anode channels, i.e., the planar single channel model is not a full 2D model. The species composition is resolved in 1D in the gas channels (along the direction of axial flow) as well as in the porous media (transverse to the direction of axial flow). For each axial position in the flow channel, the porous media is resolved across its thickness, i.e., even though the governing equations have only one independent space coordinate, it generates an overall 2D effect. In this model, the flow through the channels is assumed to be plug flow, and multi-component species transport through the porous media is represented by Dusty Gas Model (DGM). Detailed description of the single channel model is also reported elsewhere [46].

#### 2.1.1. Fluid and energy transport

Flow through fuel and air channels is assumed to be one-dimensional and laminar in nature. The plug flow equation for species continuity in the channels is given by

$$\frac{\partial \left( \rho_f Y_k \right)}{\partial t} = -\frac{\partial \left( \rho_f v Y_k \right)}{\partial z} + \frac{P_e}{A_c} J_k W_k, \quad k = 1, \ldots, K_g. \tag{1}$$

The velocity is calculated from the momentum equation

$$\frac{\partial \left( \rho_f v \right)}{\partial t} = -\frac{\partial \left( \rho_f v v \right)}{\partial z} + v \sum_{k=1}^{K_g} \frac{P_e}{A_c} J_k W_k. \tag{2}$$

where $P_e$ is the perimeter associated with the membrane electrode assembly, $\rho_f$ is the fluid density, $Y_k$ is the species mass fraction of species $k$, $v$ is the velocity, $z$ is the axial position, $t$ is the time, $W_k$ is the species molecular weight, and $A_c$ is the cross-sectional area of

the channel. Assuming constant pressure in the channels, the density is calculated from the ideal gas equation

$$p\overline{M} = \rho_f RT. \tag{3}$$

In Eqs. (1) and (2), $J_k$ is the flux at the electrode channel interface, which is calculated using the dusty gas model (DGM) as described below. The single channel model evaluates the species properties based on the stack temperature at the corresponding spatial positions. The temperature $T_f$ in the flow channels is determined from the heat balance equation

$$\frac{\partial\left(\rho_f C_{pf} T_f\right)}{\partial t} = \frac{\partial\left(v\rho_f C_{pf} T_f\right)}{\partial z} + \frac{4h}{D_h}\left(T_{stack} - T_f\right). \tag{4}$$

Here, $C_{pf}$ is the specific heat capacity of the fluid. $T_f$ and $T_{stack}$ are the temperatures of the fluid stream and solid phase, respectively. The first term on the right-hand side of Eq. (4) represents the transport of energy due to bulk fluid flow, and the second term represents the heat transfer between the channels and the solid stack structure. The heat transfer coefficient $h$, which is a local property and changes along the length of the channel, is evaluated from the Nusselt number

$$Nu = \frac{hD_h}{\lambda}, \tag{5}$$

where $D_h$ is the hydraulic diameter and $\lambda$ is the thermal conductivity of the fluid. The Nusselt number is expressed empirically as [47]:

$$Nu = 3.095 + 8.933\left(\frac{1000}{Gz}\right)^{-0.5386}\exp\left(-\frac{6.7275}{Gz}\right). \tag{6}$$

where the Graetz number, Gz, is given in terms of the Reynolds number, Re, and Prandtl number, Pr, as

$$Gz = \frac{D_h}{z}Re\,Pr. \tag{7}$$

where $z$ is the axial position along the channel.

### 2.1.2. Porous media transport

Due to geometrical considerations, species transport through the porous media is assumed to be one-dimensional along the thickness of the porous structure, i.e., transverse to the direction of flow in the channel and is given by

$$\frac{\partial\left(\phi\rho_f Y_k\right)}{\partial t} = -\frac{\partial(J_k W_k)}{\partial y} + \dot{s}_k W_k A_s. \tag{8}$$

Here, $\phi$ is the porosity, $\dot{s}_k$ is the heterogeneous molar production rate of the chemical species $k$, $y$ is the independent spatial variable along the thickness, and $A_s$ is the specific catalyst area available for surface reactions. Total density of the fluid within the porous structure can be calculated from

$$\frac{\partial\left(\phi\rho_f\right)}{\partial t} = -\sum_{k=1}^{K_g}\frac{\partial(J_k W_k)}{\partial y} + \sum_{k=1}^{K_g}\dot{s}_k W_k A_s. \tag{9}$$

In the above equations, the fluxes $J_k$ are evaluated using the DGM. According to DGM, the net species molar flux is given by [46]

$$J_k = -\left[\sum_{l=1}^{K_g}D_{kl}^{DGM}\nabla[X_l] + \left(\sum_{l=1}^{K_g}\frac{D_{kl}^{DGM}[X_l]}{D_{l,Kn}^e}\right)\frac{B_g}{\mu}\nabla p\right]. \tag{10}$$

The first term on the right-hand side of Eq. (10) represents the diffusive flux and the second term represents the viscous flux. $D_{kl}^{DGM}$ is defined as DGM diffusion coefficients given as [46]

$$D_{kl}^{DGM} = H^{-1}, \tag{11}$$

where the elements of the $H$ matrix are

$$h_{kl} = \left[\frac{1}{D_{k,Kn}^e} + \sum_{j\neq k}\frac{X_j}{D_{kj}^e}\right]\delta_{kl} + (\delta_{kl} - 1)\frac{X_k}{D_{kl}^e}. \tag{12}$$

The permeability $B_g$ in Eq. (10) is given by Kozeny–Carman relationship [50].

$$B_g = \frac{\phi^3 d_p}{72\tau(1 - \phi)^2}. \tag{13}$$

Here, $d_p$ is the particle diameter and $\tau$ is the tortuosity.
The Knudsen diffusion coefficient $D_{l,Kn}^e$.Eq. (10) is given by

$$D_{l,Kn}^e = \frac{\varepsilon}{\tau}\frac{d_p}{3}\sqrt{\frac{8RT}{\pi W_k}}. \tag{14}$$

The global charge transfer reaction at the three-phase interface can be written as:

$$H_2 + O^{2-} \Leftrightarrow H_2O + 2e^-. \tag{15}$$

The anode chemistry model adopted here emphasizes the potential of elementary heterogeneous mechanism for the steam reforming of methane on Ni catalysts. The modeling framework of heterogeneous chemistry is described in our previous reports [46,49,51]. The computational procedure used to solve the system of coupled non-linear equations follows a space marching algorithm, so that, at each axial position, the transient systems of equations are solved until a steady state solution is obtained. The initial condition at each axial position assumes the converged solution from the previous finite volume cell. More discussions about the procedure are given elsewhere [52]. Eqs. (1)–(4) and (8) form a set of differential algebraic equations at each time step, which are solved after discretization, using the solver LIMEX [55].

### 2.2. Stacks

The timescales of various processes such as kinetics, diffusion, and heat transfer occurring in an SOFC stack are different from each other, and the heat transfer process has a higher time constant compared to the rest of the processes. Therefore, it is quite rational to assume all processes but heat transfer to be in steady state. In the method adopted here, the solid phase temperature is decoupled from the fluid phase to develop the transient stack model, which solves the transient two- or three-dimensional heat conduction equation. While solving the heat conduction equation, the stack is assumed to be a porous media consisting of straight channels.

$$\rho C_p\frac{\partial T}{\partial t} = \frac{\partial}{\partial x_i}\left(\lambda_{ij}\frac{\partial T}{\partial x_j}\right) + q, \tag{16}$$

where $t$ is the time, $T$ is the temperature, $\rho$ is the density, $C_p$ is the heat capacity, $\lambda_{ij}$ is the tensor of heat conductivity, $q$ is the heat source term from the interaction with the channels. Time integration is carried out for the solid phase heat balance. At every axial position, solid phase temperature is obtained and subsequently used to calculate the reaction rates and gas phase temperature. The MEA is collectively considered as porous media by the solid structure.

## 2.3. Boundary conditions

Solving the partial differential equations requires the specification of boundary conditions at the borders of the simulation domain. Depending on the operating conditions, Dirichlet boundary conditions

$$T|_{\text{wall}} = \text{const},\qquad(17)$$

or Neumann conditions

$$k\frac{\partial T}{\partial n}\bigg|_{\text{wall}} = \Psi,\qquad(18)$$

may be used. In the above equations, the heat flux $\Psi$ in the normal direction of the border $n$ may consist of a linear heat condition term, a bi-quadratic radiation term and a constant term

$$\Psi = h(T - T_{\text{surr}}) + \varepsilon\sigma\left(T^4 - T_{\text{surr}}^4\right) + \Psi_{\text{const}}.\qquad(19)$$

Here, $\sigma$ is the Stefan–Boltzmann constant. The heat transfer coefficient $h$, the emissivity $\varepsilon$, and the temperature of the surroundings $T_{\text{surr}}$ have to be specified as model parameters. Nevertheless, the stack model may easily be coupled with an arbitrary combination of user-defined Dirichlet or Neumann boundary conditions. The initial condition used in this case refers to the initial temperature of the solid structure/stack. Physically, it is the operating temperature to which the stack is heated up before use, since SOFCs operate at a range of temperatures from 600 to 1000 °C.

## 2.4. Heat source term

The heat source term is derived from the simulation of individual cells. For systems with nearly constant pressure, the energy conservation can be expressed in terms of enthalpy. Constant pressure is assumed while modeling the individual channels. Then, the enthalpy flux in the channel $\dot{H}_{\text{channel}}$ can only be changed along the channel axis by heat exchange with the stack. If the channel density is $\gamma$ (channels per unit area of the cross-section), the source term can be expressed as

$$q = -\gamma\cdot\frac{\partial\dot{H}_{\text{channel}}}{\partial x} + Q_{\text{ohmic}}.\qquad(20)$$

Here, $Q_{\text{ohmic}}$ is the heat release due to ohmic heating within the electrolyte. By inclusion of enthalpy of formation into its definition, $\dot{H}_{\text{channel}}$ does not change due to electrochemical oxidation.

## 3. Solution methods

### 3.1. Discretization of the PDE

The stack is assumed to be a continuum, whose transient temperature field is described by the heat conduction equation Eq. (16). This differential equation shall be solved for the two- and three-dimensional cases. We assume that all channels of the unit cells within the stack are parallel, denoted by the direction of the $x$-axis.

The two- or three-dimensional fields need to be discretized in order to solve the differential equations. Here, we chose a finite volume method. For the two-dimensional case, we always use an orthogonal grid. In case of three dimensions, the grid in the $yz$-plane can be unstructured and consisting of arbitrarily shaped triangles and quadrilaterals. This grid is extended orthogonally into the $x$-direction. Thus, the finite volume elements are three- or four-sided prisms.

Due to the orthogonality of the grid with respect to the direction of the unit cell channels, it is easy to distinguish between the axial and radial direction for the heat conduction. In order to account for structure dependent differences, we applied separate heat conductivity coefficients to the axial and the radial directions, $\lambda_{\text{axial}}$ and $\lambda_{\text{radial}}$, respectively.

The heat source term $q$ is obtained from the simulations of individual cells. Each row of grid cells in the axial direction defines a temperature profile that is used as the boundary condition for the channels crossing these grid cells. Thus, the number of cells of the grid in the $y$-direction or in the $xz$-plane defines a maximum number of different temperature profiles for the unit cell simulations.

In order to resolve the heat field, Eq. (16) is discretized by finite volume method. For a partial differential equation (PDE) of the form

$$\rho C_{\text{p}}\frac{\partial T}{\partial t} = \frac{\partial}{\partial x_i}\left(k\frac{\partial T}{\partial x_j}\right),\qquad(21)$$

we integrate over a channel and apply Stokes' integral theorem to get

$$V\cdot\rho C_{\text{p}}\frac{\partial T}{\partial t} = \sum_{\text{faces}}\Phi_{\text{face}}\qquad(22)$$

Here, $\Phi_{\text{face}}$ is the heat flow through a face of the channel. The channel itself shall be denoted by index $0$ and its neighbor by index $n$. In the axial direction, we can directly use a finite difference approximation of the temperature gradient because of the orthogonality of the grid

$$\Phi_{\text{ax}} = -kA_{\text{face}}\left(\frac{T_0 - T_n}{x_0 - x_n}\right).\qquad(23)$$

In radial direction, the gradient can be approximated by the temperatures $T_0$, $T_n$, $T_A$, $T_B$, as shown in Fig. 1. The heat flow then becomes

$$\Phi_{\text{rad}} = \Phi_{AB}\cdot\Delta x.\qquad(24)$$

with

$$\Phi_{AB} = k\cdot\begin{pmatrix}\dfrac{\partial T}{\partial y}\\[4pt]\dfrac{\partial T}{\partial z}\end{pmatrix}\cdot\begin{pmatrix}-(z_B - z_A)\\(y_B - y_A)\end{pmatrix}.\qquad(25)$$

This expression can be simplified into

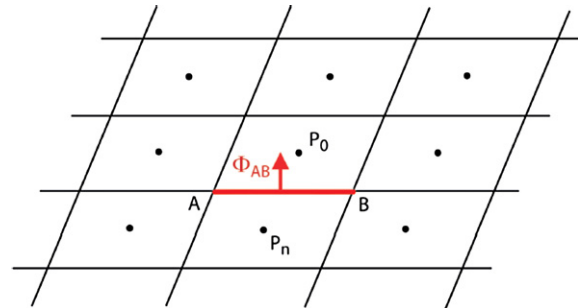$$\Phi_{AB} = -k(\alpha(T_0 - T_n) + \beta(T_B - T_A)).\qquad(26)$$

with



**Fig. 1.** Depiction of gradient approximation in radial direction by specified temperatures.

$$\alpha = \frac{\overrightarrow{AB}^2}{\left| \overrightarrow{AB} \times \overrightarrow{P_nP_0} \right|}. \tag{27}$$

$$\beta = \frac{\overrightarrow{AB} \cdot \overrightarrow{P_nP_0}}{\left| \overrightarrow{AB} \times \overrightarrow{P_nP_0} \right|}. \tag{28}$$

The parameters $\alpha$ and $\beta$ only have to be calculated once for the grid. As a result of finite volume approximation, these grid-based parameters depend on $P_0$, $P_n$, which refer to centers of adjacent cells, and $A$, $B$, which are nodes of the same cell. With them, the right-hand side of the PDE is transformed into a system of algebraic equations.

### 3.2. Choosing representative channels

Calculating individual channel flow fields is the most time consuming step in a stack simulation. In order to reduce the computational cost, only representative channels are chosen for detailed simulation. Due to the representation of the stack by a discrete grid, there is a unique channel boundary temperature profile for each axial row of grid points. A finite number of variables (for instance, only temperature $T$ is considered in this case) completely define the parameters for a channel simulation, i.e., the calculation of source terms can be viewed as a mapping from the input vector

$$x^k = \left( T^k_{\text{wall},1}, \ldots, T^k_{\text{wall},n} \right). \tag{29}$$

of the $k$th discretized channel to an output vector containing the heat source terms $q$ of the respective grid points. This mapping can be expected to be continuous; channels with similar input vectors shall be similar in source terms. For the identification of similar channels, an agglomerative cluster algorithm is applied.

A weight $w^k$ can be assigned to each vector $x^k$ that accounts for the absolute number of channels represented by $x^k$, which is proportional to the size of the corresponding stack area. In addition, a distance function $d(x^i, x^j)$ is necessary, for which a normalized maximum norm is chosen:

$$d\left(x^i, x^j\right) = \max\left( d_T\left(T^i_{\text{wall},1}, T^j_{\text{wall},1}\right), \ldots, d_T\left(T^i_{\text{wall},n}, T^j_{\text{wall},n}\right)\right). \tag{30}$$

with distance functions

$$d_T\left(T^i, T^j\right) = \frac{\left| T^i - T^j \right|}{\delta T} \tag{31}$$

i.e., temperatures are normalized with respect to a temperature difference $\delta T$. The agglomerative cluster algorithm, illustrated in Fig. 2, can be sketched as follows:

1. Find the minimum $d^* = d(x^*, x^*) = \min_{i \neq j}(d(x^i, x^j))$.
2. Stop if $d^* > 1$,
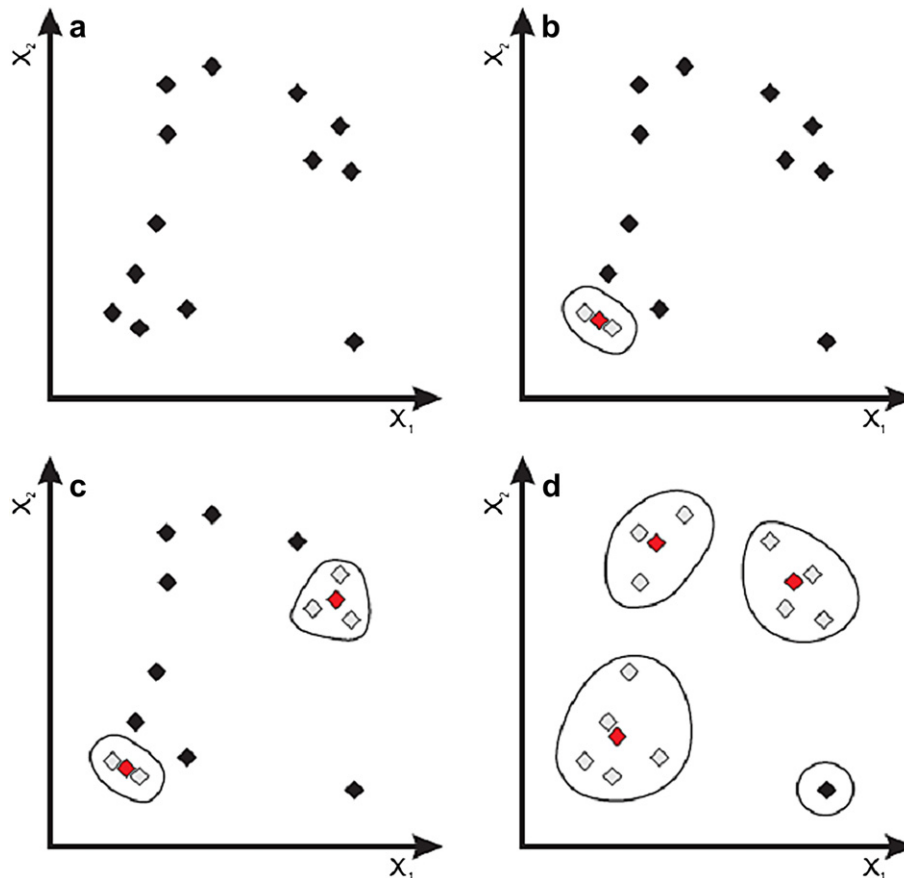3. Let $x^* = (w^* x^* + w^* x^*)/(w^* + w^*)$ and $w^* = w^* + w^*$.



**Fig. 2.** Agglomerative cluster algorithm. (a) Given set of data points. (b) Join two data points into one cluster. (c) After the third agglomeration step, two clusters have been formed. (d) Final representation of the data by four clusters.

4. Eliminate $(x^*, w^*), (x^*, w^*)$ and replace by $(x^*, w^*)$.
5. Go to 1.

The remaining $x^k$ are the input vectors for representative channels. All input vectors in one cluster are associated with the same output source terms. Since the channel equations are not explicitly time-dependent, the number of channel calculations can be further reduced by including the $x^k$ of previously calculated channels into the clustering and reusing their results. A schematic representation of the coupling between the solid section and the individual channel is shown in Fig. 3. The stack code is available as a part of DETCHEM software [48].

## 4. Results and discussion

For demonstration purposes, we consider a stack having an active area of 10 cm × 10 cm and consisting of 30 cells in co-flow configuration. The fuel and air channels are assumed to be of 1 mm² cross-sectional area. All the physical parameters and thermal properties used to describe the stack are given in Table 1. The electrochemical model parameters used for the calculations are shown in Table 2. The exchange current density formulations are taken from Ref. [49]. A detailed discussion about the electro-chemical model used in this study is enunciated in Ref. [46,49]. However, the exchange current density parameters are adjusted to produce ~0.72 V at 300 mA cm⁻². Adiabatic and Neumann boundary conditions are implemented for the present calculation. It should be noted that the time constants pertaining to electro-chemistry, diffusion, internal impedance, mass transfer and temperature dynamics are specific to the model parameters used in this study.

As described in the previous section, either the voltage or the current can be fixed to estimate the rest of the electrochemical parameters. Therefore, two different transient responses following load changes are studied here: (i) load change at constant current and (ii) load change at constant voltage. For both cases, the stack is
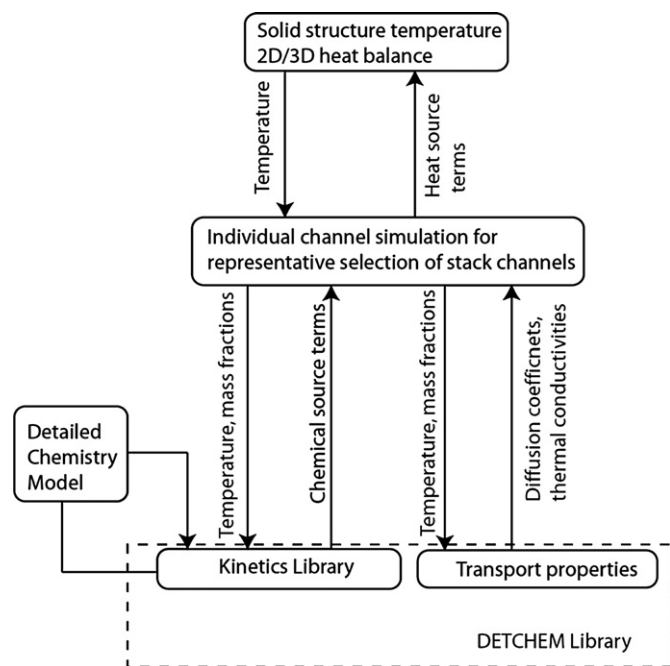
**Table 1**
Stack component parameters and properties.

| Physical | Flow channels | |
|---|---|---|
| | Length (m) | 0.1 |
| | Height (m) | $1 \times 10^{-3}$ |
| | Width (m) | $1 \times 10^{-3}$ |
| | Anode | |
| | Thickness (μm) | 750 |
| | Porosity (%) | 35 |
| | Tortuosity | 3.5 |
| | Particle diameter (μm) | 2.5 |
| | Pore diameter (μm) | 1.0 |
| | Specific area (m⁻¹) | $1.080 \times 10^5$ |
| | Cathode | |
| | Thickness (μm) | 30 |
| | Porosity (%) | 35 |
| | Tortuosity | 3.5 |
| | Particle diameter (μm) | 2.5 |
| | Pore diameter (μm) | 1.0 |
| | Specific area (m⁻¹) | $1.080 \times 10^5$ |
| | Electrolyte | |
| | Thickness (μm) | 15 |
| Thermal | Solid/stack | |
| | Specific heat capacity (J kg⁻¹ K) | 440 |
| | Density (kg m⁻³) | 5940 |
| | Thermal conductivity (J m⁻¹ s K) | 1.86 |
| | Insulator | |
| | Specific heat capacity (J kg⁻¹ K) | 1047 |
| | Density (kg m⁻³) | 480 |
| | Thermal conductivity (J m⁻¹ s K) | 0.059 |
| | Thermal emissivity | 0.09 |
| | Convective coefficient insulator/surrounding (W m⁻² K⁻¹) | 2 |

initially assumed to be at 800 °C. Inlet fuel and air are assumed to be at 800 °C and 750 °C, respectively.

### 4.1. Constant current

#### 4.1.1. Adiabatic condition

Fig. 4 displays the transient response in the stack temperature for cells operating at constant current. From the initial condition, the temperature distribution in the stack reaches steady state after ~14.5 min. At $t = 80$ min, a step change in current from 0.3 A cm⁻² to 0.4 A cm⁻² is introduced. As expected, the stack temperature increases with the step increase in current and reaches steady state after another ~17 min. These response times correspond well with the values reported by Ivers-Tiffée et al. [33]. The corresponding changes in cell voltage and reversible voltage are shown in Fig. 5. The reversible potential decreases following the step change in current due to the increase in temperature. However, subsequent to the step change in current from 300 mA cm⁻² to 400 mA/cm², the cell voltage first decreases before reaching steady state. The initial decrease in cell potential occurs due to the following reasons.

- An increase in current leads to an increase in overpotential losses, because the stack temperature at the time of step



**Fig. 3.** Illustration of coupling between the solid structure and the channel.

**Table 2**
Electrochemical model/input parameters.

| | |
|---|---|
| Anode asymmetry factor ($\beta_a$) | 0.5 |
| Cathode asymmetry factor ($\beta_c$) | 0.5 |
| | |
| *Exchange current density parameters* | |
| Pre-exponential for H₂ oxidation ($k_{H2}$) (A cm⁻²) | $1.07 \times 10^4$ |
| Pre-exponential for O₂ reduction ($k_{O2}$) (A cm⁻²) | $5.19 \times 10^3$ |
| Activation energy for H₂ oxidation ($E_{H2}$) (J mol⁻¹) | $87.8 \times 10^3$ |
| Activation energy for O₂ reduction ($E_{O2}$) (J mol⁻¹) | $88.6 \times 10^3$ |

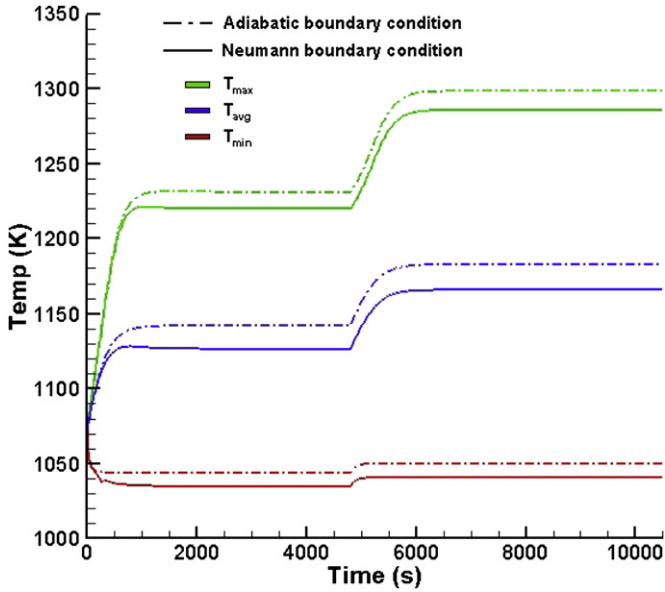**Fig. 4.** Maximum, minimum, and average temperature in the stack for step change in current from 0.3 A cm$^{-2}$ to 0.4 A cm$^{-2}$.



**Fig. 6.** Anode activation overpotential following a step change in current from 0.3 A cm$^{-2}$ to 0.4 A cm$^{-2}$.



**Fig. 7.** Cathode activation overpotential following a step change in current from 0.3 A cm$^{-2}$ to 0.4 A cm$^{-2}$.

change still corresponds to the steady state temperature at 300 mA cm$^{-2}$.

• The activation losses gradually decrease as the temperature approaches the new steady state.

In short, the under-shoot in cell potential originates from the over-shoot in activation losses following the step change. The corresponding transient response of activation losses at the anode and cathode are displayed in Figs. 6 and 7, respectively.

In Fig. 8, we see the response of the stack temperature to step changes in current density from 0.3 A cm$^{-2}$ and 0.5 A cm$^{-2}$ to a new steady state value of 0.4 A cm$^{-2}$. The response times of the system, after the respective step changes are introduced, are the same and equate to ∼17 min. Thus, we observe that the response times remain independent of the magnitude of load introduced. This phenomenon was also observed by Achenbach [37].
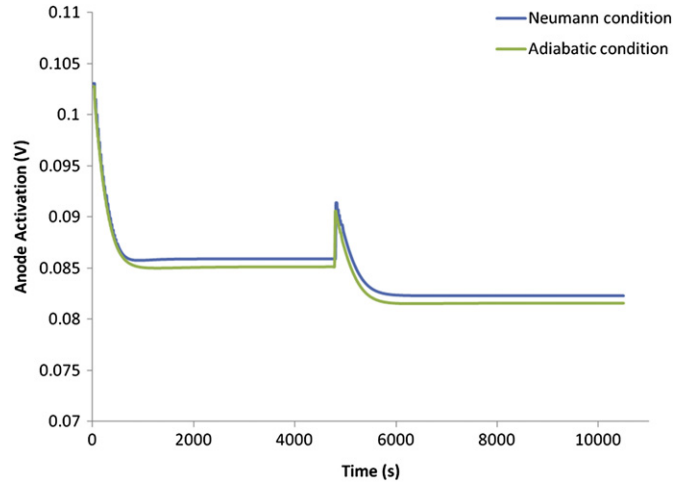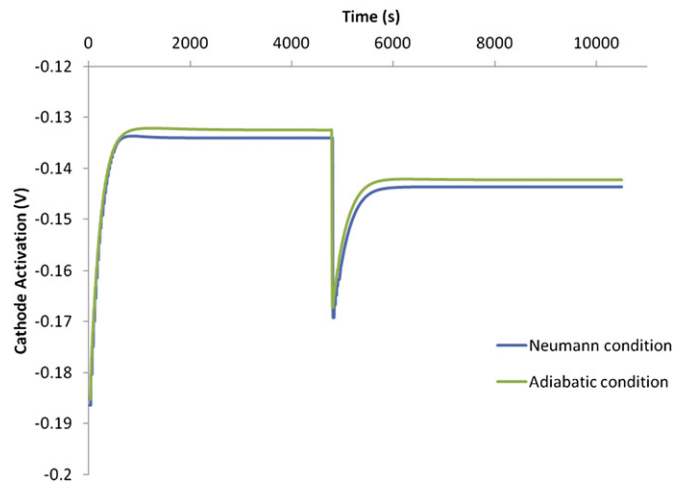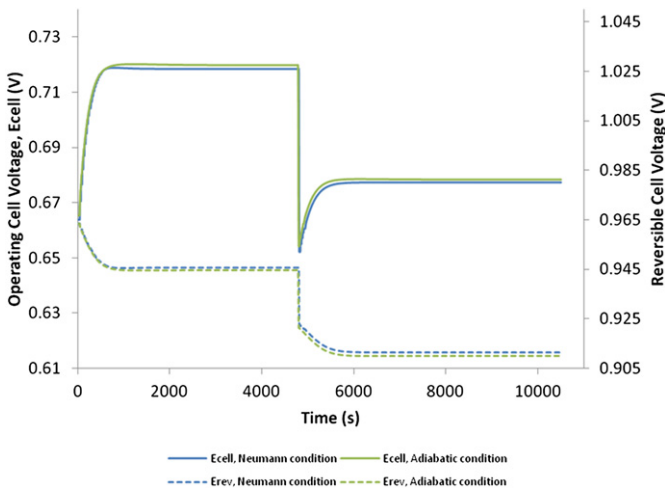


**Fig. 5.** Cell potential and reversible potential following a step change in current from 0.3 A cm$^{-2}$ to 0.4 A cm$^{-2}$.
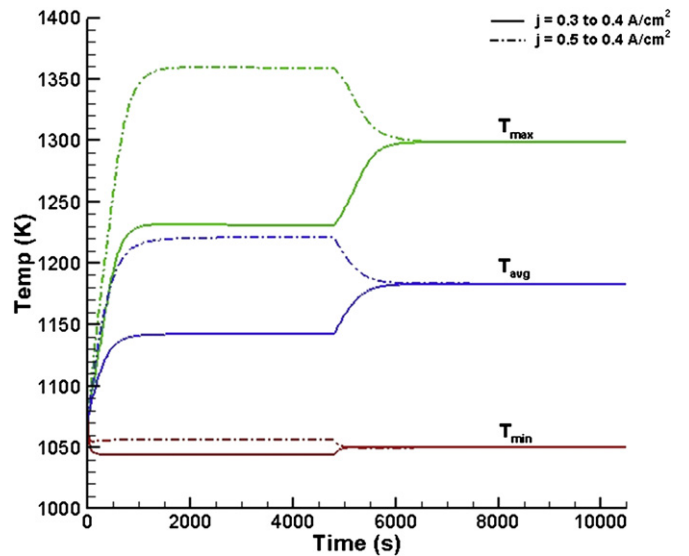


**Fig. 8.** Transient temperature distribution during load change from $j = 0.3$ or $j = 0.5$ to $j = 0.4$ A cm$^{-2}$.
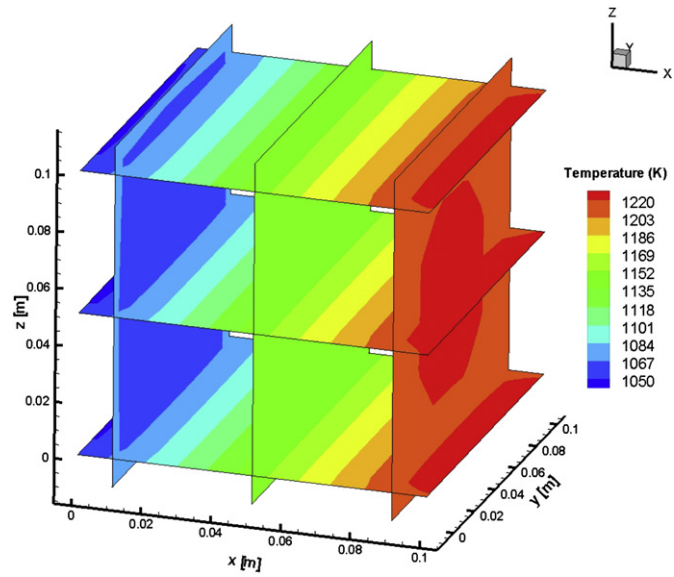
**Fig. 9.** Temperature distribution in the 3D stack (solid phase) at different surface planes, along and across the flow direction, at $t = 60$ min during adiabatic operation.

The temperature distribution in the stack at different planes along and across the flow direction, after the first steady state, is displayed in Fig. 9. As expected, the temperatures in the stack increase in a monotonic manner along the flow direction due to the combined effect of exothermic cell reactions and the current consumed by the internal cell resistance. However, uniform profiles are observed across the direction of flow because of the relatively thin PEN structure and the radial thermal conductivity of the solid. Also, the insulator seems to have minimal effect on the internal temperature distribution of the system. It should be noticed that the model has a limitation that does not account for individual mechanical components in the stack. It is a lumped parameter model as far as individual mechanical components are concerned, and therefore, it is assumed that the entire stack has the same thermal properties.
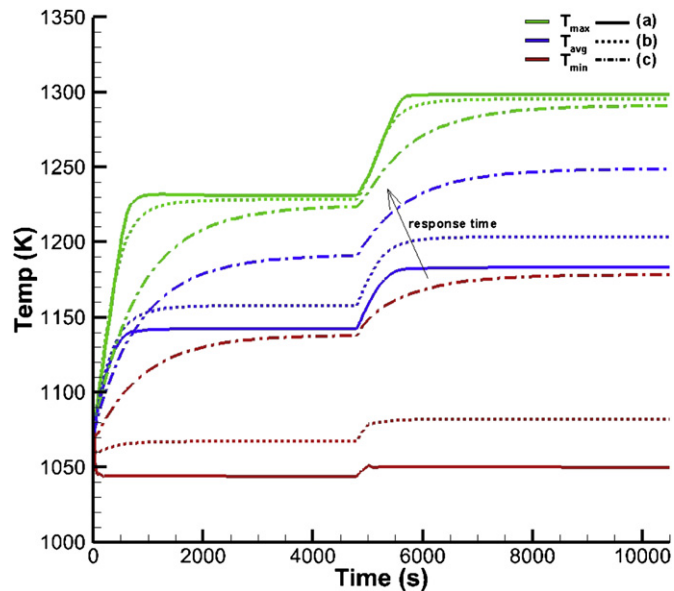
**Table 3**
Solid structure/stack material properties.

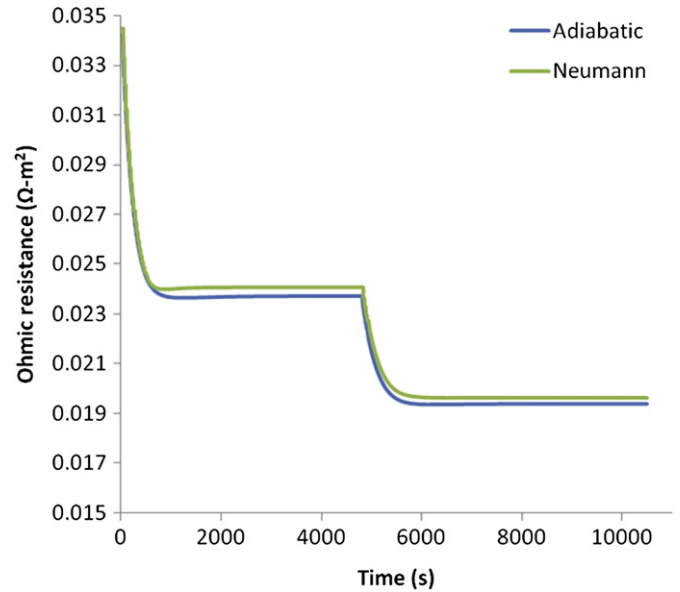| Material | Thermal conductivity ($\lambda - \mathrm{W\,mK^{-1}}$) | Thermal diffusivity ($\alpha$ -$\mathrm{mm^2\,s^{-1}}$) |
|---|---|---|
| (a) | 1.86 | 0.716 |
| (b) | 5.86 | 2.466 |
| (c) | 27 | 6.923 |



**Fig. 11.** Ohmic polarization following a step change in current from 0.3 A cm$^{-2}$ to 0.4 A cm$^{-2}$.

During the calculations, we observed that the time constants for the dynamic responses are strongly dependent on thermal diffusivity ($\lambda/\rho C_p$). Lower thermal diffusivity led to a faster response or to a shorter time constant, which can be attributed to mass transfer
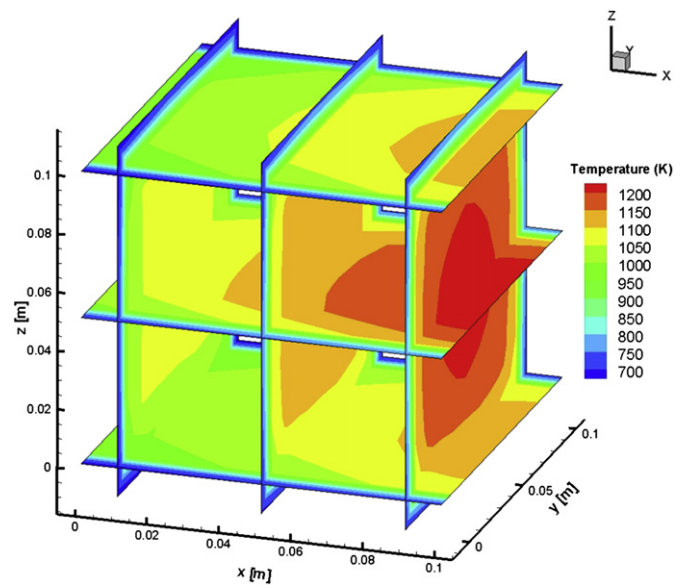


**Fig. 10.** Illustration of solid structure material property *vs.* response time.



**Fig. 12.** Temperature distribution in the 3D stack (solid phase) at different surface planes, along and across the flow direction, at $t = 60$ min during computation with an imposed Neumann condition.
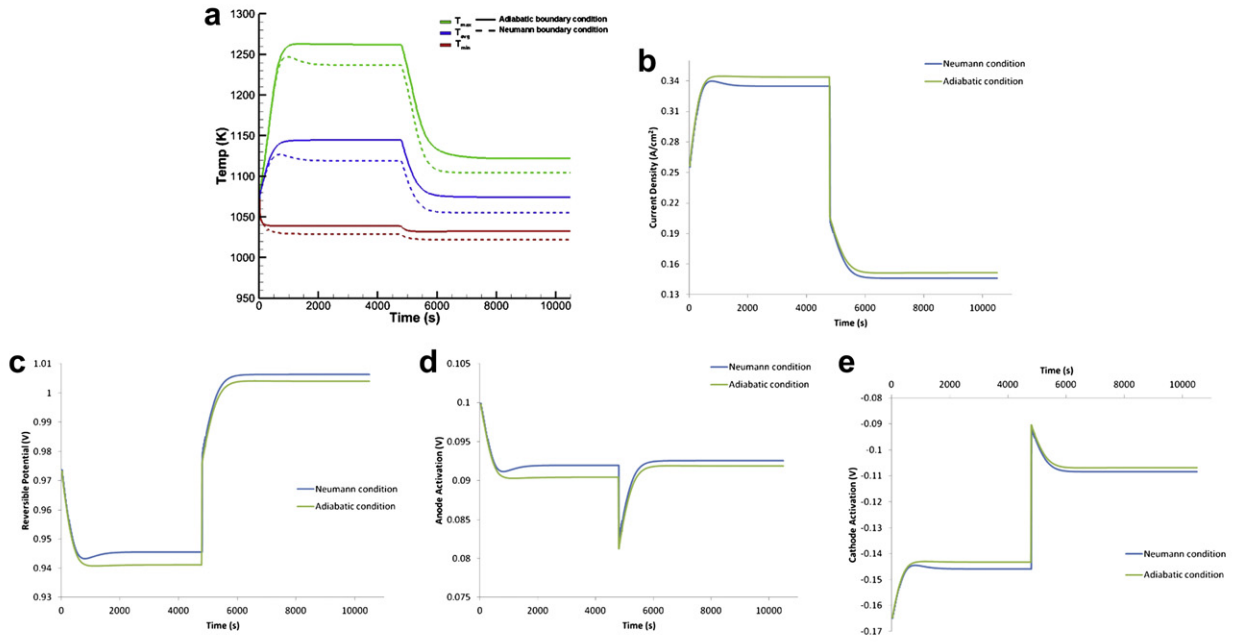
**Fig. 13.** (a) Maximum, minimum, and average temperature in the stack for step change in voltage from 0.7 V to 0.8 V. (b) Average current density following a step change in voltage from 0.7 V to 0.8 V. (c) Reversible cell potential following a step change in voltage from 0.7 V to 0.8 V. (d) Anode activation overpotential following a step change in voltage from 0.7 V to 0.8 V. (e) Cathode activation overpotential following a step change in voltage from 0.7 V to 0.8 V.
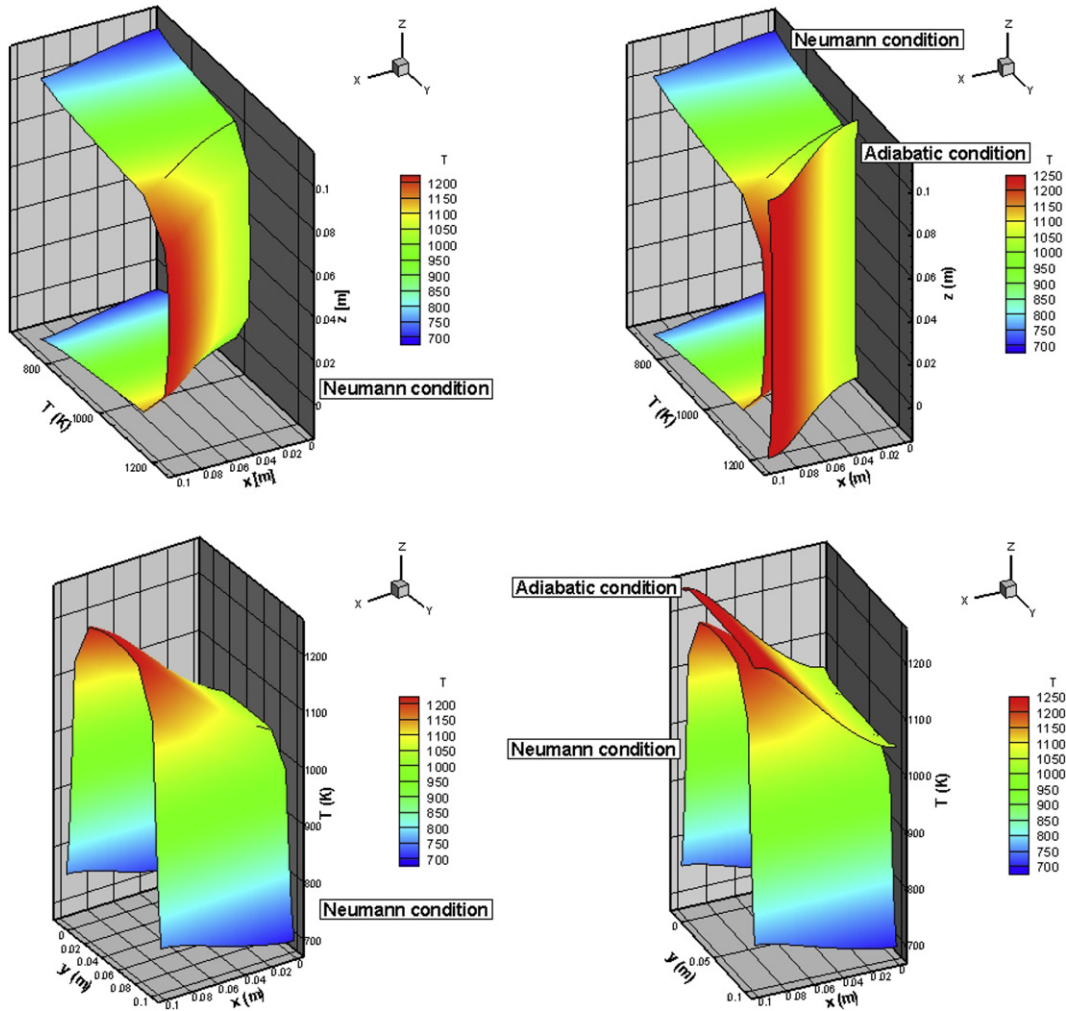


**Fig. 14.** Internal steady state temperature distribution of the stack before step change in voltage from 0.7 V to 0.8 V.
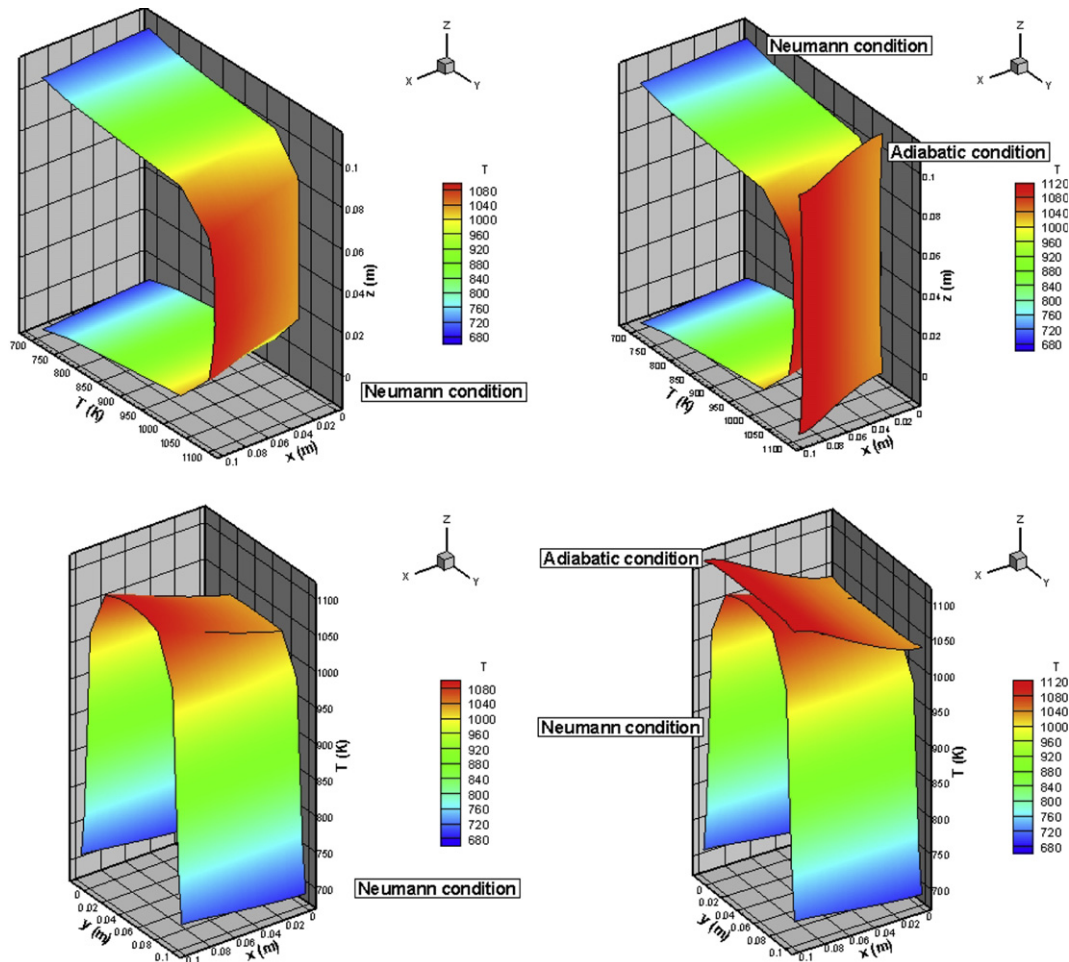
**Fig. 15.** Internal steady state temperature distribution of the stack after step change in voltage from 0.7 V to 0.8 V.

dynamics. This was also observed by Achenbach [37]. It might be possible that Li et al. [32] used high thermal diffusivity for their model calculations, which led to very high response times. This phenomenon is depicted in Fig. 10, with the corresponding solid stack structure properties listed in Table 3. A number of other stack operating conditions, such as convection and radiation losses, and the effect of re-circulation zones at the inlet and outlet faces/manifolds are not discussed here.

### 4.1.2. Neumann condition

The Neumann condition, as described in Table 1, is applied at the four faces of the stack, barring the inlet and outlet face which are kept adiabatic. As shown in Fig. 4, the temperature distribution reaches steady state, from the initial value, at ∼15 min. A step change in current from 0.3 A cm$^{-2}$ to 0.4 A cm$^{-2}$ at $t = 80$ min is introduced, due to which the temperature distribution in the stack reaches a new steady state value in ∼18.5 min. This is due to the dependence of response time on operating conditions.

The heat loss at the surface of the stack results in a decrease in the magnitude of its temperature distribution, which leads to the production of relatively low amount of waste heat. This causes the average cell temperature to decrease, which manifests itself as an increase in ohmic polarization, resulting in a lower operating cell voltage as described in Fig. 11. The reversible potential, which is obtained from the Nernst equation, is higher due to the lower amount of heat generated by the cell ($T\Delta S$) that operates reversibly. This increases the amount of free energy available to the system. This phenomenon is shown in Fig. 5.

The internal temperature distribution in the stack, at different planes after the attainment of the first steady state, is shown in Fig. 12. This is a pre-dominant factor in determining any induced thermal stresses in the materials positioned at different locations of the system. Furthermore, as a result of heat loss/flux at the boundaries, the distinct temperature contours are formed due to the increase in temperature gradients in the Y and Z directions. This shows the importance of 3D modeling for determining how temperature dynamics play an important role in the transient responses of a SOFC system.

### 4.2. Constant voltage

#### 4.2.1. Adiabatic condition

Fig. 13a describes the transient response in temperature for cells operating at constant voltage. Here, the initial steady state is achieved in ∼15 min, and at $t = 80$ min, a step change in voltage from 0.7 V to 0.8 V is introduced. The increase in cell potential decreases the average current from the stack, and as expected, the stack temperature reaches a new lower steady state value in about ∼18 min. The corresponding transient responses in current and reversible potential are displayed in Fig. 13b and c, respectively. As usual, the decrease in temperature following the step increase in voltage leads to an increase in the reversible potential. The current density drops from ∼340 mA cm$^{-2}$ following the step change in voltage, and then gradually assumes a new steady state value of ∼150 mA cm$^{-2}$. Nevertheless, the step change in voltage leads to an under-shoot in activation losses. At the time of step change, the

temperature in the stack corresponds to that of $\sim 340\,\mathrm{mA\,cm^{-2}}$; however, the drop in current density at higher stack temperature leads to lower activation losses, which in turn corresponds to the point of under-shoot. Nonetheless, as the stack temperature assumes a new lower steady state value, the activation losses increase and asymptotically reach a new steady state value. The anode and cathode activation losses are displayed in Fig. 13d and e, respectively.

### 4.2.2. Neumann condition

The thermal properties of the insulator and the Neumann condition at the stack surface are described in [54]. Fig. 13a shows that the time taken to reach steady state from the initial condition is $\sim 17$ min. At $t = 80$ min, a step change in voltage from 0.7 V to 0.8 V is introduced, causing the stack temperature to attain a new steady state value in about $\sim 17$ min. The ohmic polarization increases as the operating temperature decreases, which results in the decrease of current density at a given cell voltage, as shown in Fig. 13b. Consequently, the reversible potential increases as shown in Fig. 13c.

The 3D contour plots of the cell stack describe the steady state internal temperature distributions before and after the step change in voltage is introduced, which are shown in Figs. 14 and 15, respectively. These figures represent the temperature profiles of the cell located at the center of the stack. A comparison with the adiabatic case provides a comprehensible idea about the differences in the magnitudes of temperature gradients for the same model input parameters. It can be seen that the adiabatic condition results in a smaller temperature gradient at the boundaries compared to the case involving heat loss at the boundaries. The resulting temperature distribution arises due to the net effect of heat absorbed or released as a result of heterogeneous chemical reactions, heat release due to the electrochemical reactions at the TPB, resistive heating within the electrolyte, convective heat transfer to and from the channels, radiation heat transfer with the interconnects, and also heat loss at the stack boundaries in the case of an imposed Neumann condition. The temperature decline at the inlet is attributed to endothermic reforming reactions. It is evident that the temperature increases in the axial direction, due to exothermic cell reactions, along with the air and fuel channel temperature. This in turn reflects in the gradual increase of insulator temperature from the inlet to the outlet face. Each cell's temperature distribution also depends on its position within the stack. This affects the dynamics of almost all other mechanisms. During our simulations, when considering different materials for insulation at the stack surface, we observed that the choice of insulation layer was mainly responsible for controlling the surface temperature of the system that determined the amount of heat available for transfer to the surroundings.

## 5. Conclusion

We have developed a novel numerical algorithm for the modeling of 3D/2D SOFC stacks. The model is demonstrated with a reformate fuel composition for a co-flow cell configuration. Instead of simulating every individual cell in the stack, only representative ones based on the cluster algorithm are chosen for detailed simulation. This approach dramatically reduces the computation time required for stack simulation. Furthermore, we also studied the dynamics of the stack during two different transient responses to load changes: constant current and constant voltage. It was observed that the adiabatic/Neumann cases at the borders of the simulation domain yielded almost the same response times between the two steady states, for both types of load changes. The limitation of the model is the higher level of

abstraction related to the individual mechanical components of the stack. Nevertheless, the novel model and computational tool can assist in a better understanding of heat balances in SOFC stacks, even when operated with other fuels than pure hydrogen.

## References

[1] C. Bao, Y.X. Shi, C. Li, N.S. Cai, Q.Q. Su, International Journal of Hydrogen Energy 35 (2010) 2894–2899.
[2] D. Cocco, V. Tola, Energy Conversion and Management 51 (2010) 623.
[3] P. Kazempoor, V. Dorer, F. Ommi, International Journal of Hydrogen Energy 34 (2009) 8630–8644.
[4] A. Salogni, P. Colonna, Applied Thermal Engineering 30 (2010) 464–477.
[5] A. Traverso, L. Magistri, A.F. Massardo, Energy 35 (2010) 764–777.
[6] D. Vera, F. Jurado, Behavior of SOFC based generation systems in distributed generation, 2009, in: International Conference on Clean Electrical Power, IEEE, New York, 2009.
[7] S. Vivanpatarakij, N. Laosiripojana, W. Kiatkittipong, A. Arpornwichanop, A. Soottitantawat, S. Assabumrungrat, Chemical Engineering Journal 147 (2009) 336–341.
[8] Z.T. Yu, J.T. Han, X.Q. Cao, W. Chen, B. Zhang, International Journal of Hydrogen Energy 35 (2010) 2703–2707.
[9] M. Santin, A. Traverso, L. Magistri, Applied Energy 86 (2009) 2204–2212.
[10] M. Lang, C. Auer, A. Eismann, G. Schiller, P. Szabo, ECS Transactions 7 (2007) 85–94.
[11] S.B. Lee, K.S. Yun, T.H. Lim, R.H. Song, D.R. Shin, ECS Transactions 7 (2007) 187–191.
[12] P.H. Lin, C.W. Hong, Journal of Power Sources 187 (2009) 517–526.
[13] H. Timmermann, W. Sawady, R. Reimert, E. Ivers-Tiffée, Journal of Power Sources 195 (2010) 214–222.
[14] Z.W. Wang, J.O. Berghaus, S. Yick, C. Deces-Petit, W. Qu, R. Hui, R. Maric, D. Ghosh, Journal of Power Sources 176 (2008) 90–95.
[15] M. Santarelli, M. Cabrera, M. Cali, Journal of Fuel Cell Science and Technology 7 (2010) 11.
[16] M. Sorrentino, C. Pianese, Journal of Fuel Cell Science and Technology 6 (2009) 12.
[17] R.J. Braun, M. Gummalla, J. Yamanis, Journal of Fuel Cell Science and Technology 6 (2009) 10.
[18] S.K. Dong, B.T. Yun, D.K. Lee, Design and Numerical Study for 1kw Tubular SOFU APU System, vol 12, ECS Transactions Electrochemical Society Inc, Pennington, 2008, 701–706 pp.
[19] A. Lindermeir, S. Kah, S. Kavurucu, M. Muhlner, Applied Catalysis B – Environmental 70 (2007) 488–497.
[20] M.F. Serincan, U. Pasaogullari, N.M. Sammes, A computational analysis to identify the current density characteristics of a micro-tubular solid oxide fuel cell, in: Proceedings of the 6th International Conference on Fuel Cell Science, Engineering, and Technology – 2008, American Society of Mechanical Engineers, New York, 2008.
[21] S. Campanari, P. Iora, Journal of Power Sources 132 (2004) 113–126.
[22] S. Campanari, P. Iora, Fuel Cells 5 (2005) 34–51.
[23] M.F. Serincan, U. Pasaogullari, N.M. Sammes, Journal of Power Sources 194 (2009) 864–872.
[24] P. Aguiar, C. Adjiman, N. Brandon, Journal of Power Sources 147 (2005) 136–147.
[25] H.L. Cao, L. Xi, Z.H. Deng, Q. Yi, Modeling for electrical characteristics of solid oxide fuel cell based on fractional calculus, in: , 21st Chinese Control and Decision Conference, vols. 1–6, IEEE, New York, 2009.
[26] Y.T. Qi, B. Huang, K.T. Chuang, Journal of Power Sources 150 (2005) 32–47.
[27] Y.T. Qi, B. Huang, J.L. Luo, Chemical Engineering Science 61 (2006) 6057–6076.
[28] D. Bhattacharyya, R. Rengaswamy, Dynamic modeling and system identification of a tubular solid oxide fuel cell (TSOFC), in: Proceedings of the American Control Conference, IEEE, New York, 2009, pp. 2672–2677.
[29] H.L. Cao, Z.H. Deng, X. Li, J. Yang, Y. Qin, International Journal of Hydrogen Energy 35 (2010) 1749–1758.
[30] W.X. Bi, D.F. Chen, Z.J. Lin, International Journal of Hydrogen Energy 34 (2009) 3873–3884.
[31] N. Lu, Q. Li, X. Sun, M.A. Khaleel, Dynamic modeling in solid-oxide fuel cells controller design, in: Power Engineering Society General Meeting, IEEE, New York, 2007, pp. 234–240.
[32] J. Li, G.Y. Cao, X.J. Zhu, H.Y. Tu, Journal of Power Sources 171 (2007) 585–600.
[33] E. Ivers-Tiffée, A. Weber, K. Schmid, V. Krebs, Solid State Ionics 174 (2004) 223–232.
[34] H.B. Huo, X.J. Zhu, G.Y. Cao, Journal of Power Sources 162 (2006) 1220–1225.

[35] V. Lawlor, S. Griesser, G. Buchinger, A.G. Olabi, S. Cordiner, D. Meissner, Journal of Power Sources 195 (2010) 936.
[36] E. Achenbach, Journal of Power Sources 49 (1994) 333–348.
[37] E. Achenbach, Journal of Power Sources 57 (1995) 105–109.
[38] J. Padullés, G.W. Ault, J.R. McDonald, Journal of Power Sources 86 (2000) 495–500.
[39] F. Jurado, Journal of Power Sources 129 (2004) 205–215.
[40] N. Lu, Q. Li, X. Sun, M.A. Khaleel, Journal of Power Sources 161 (2006) 938–948.
[41] A. Murshed, B. Huang, K. Nandakumar, Journal of Power Sources 163 (2007) 830–845.
[42] P. Iora, P. Aguiar, C.S. Adjiman, N.P. Brandon, Chemical Engineering Science 60 (2005) 2963–2975.
[43] D.J. Hall, R.G. Colclaser, IEEE Transactions on Energy Conversion 14 (1999) 749–753.
[44] P.H. Lin, C.W. Hong, Journal of Power Sources 160 (2006) 1230–1241.
[45] B. Tu, Y. Dong, M. Cheng, Z. Tian, Q. Xin, in: F. Noronha, M. Schmal, E.F.S. Aguiar (Eds.), Natural Gas Conversion VIII, Elsevier, 2007, pp. 43–48.
[46] H. Zhu, R.J. Kee, V.M. Janardhanan, O. Deutschmann, D.G. Goodwin, Journal of Electrochemical Society 152 (2005) A2427–A2440.
[47] R.E. Hayes, S.T. Kolaczkowski, Introduction to Catalytic Combustion, Gordon and Breach Science Publishers, Amsterdam, 1997, p. 316–317.
[48] O. Deutschmann, S. Tischer, S. Kleditzsch, V.M. Janardhanan, C. Correa, D. Chatterjee, N. Mladenov, H.D. Mihn, DETCHEM Software Package, 2.3 Ed. (2010).www.detchem.com Karlsruhe.
[49] V.M. Janardhanan, O. Deutschmann, Journal of Power Sources 162 (2006) 1192–1202.
[50] J. Bear, Dynamics of Fluids in Porous Media, American Elsevier, New York, 1972.
[51] E.S. Hecht, G.K. Gupta, H. Zhu, A.M. Dean, R.J. Kee, L. Maier, O. Deutschmann, Applied Catalysis A General 295 (2005) 40–51.
[52] V.M. Janardhanan, O. Deutschmann, Chemical Engineering Science 62 (2007) 5473–5486.
[53] P. Kazempoor, F. Ommi, V. Dorer, Journal of Power Sources 196 (2011) 8948–8954.
[54] X. Xue, J. Tang, N. Sammes, Y. Du, Journal of Power Sources 142 (2005) 211–222.
[55] P. Deuflhardt, E. Hairer, J. Zugk, Numerische Mathematik 51 (1987) 501–516.

## Nomenclature

$A_c$: area of cross-section of flow channels (m$^2$)
$A_s$: specific area (m$^{-1}$)
$B_g$: permeability (m$^2$)
$C_p$: specific heat (J kg$^{-1}$ K$^{-1}$)
$d_p$: particle diameter (m)
$D$: diffusivity (m$^2$ s$^{-1}$)
$D_e^{kl}$: effective binary diffusion (m$^2$ s$^{-1}$)
$D_h$: hydraulic diameter (m)
$D_{f,Kn}^e$: effective Knudsen diffusion (m$^2$ s$^{-1}$)

$E_{cell}$: cell voltage (V)
$F$: Faraday number (C mol$^{-1}$)
$Gz$: Graetz number
$h$: heat transfer coefficient (J m$^{-2}$ K$^{-1}$ s$^{-1}$); specific enthalpy (J kg$^{-1}$)
$H_c$: channel height (m)
$\Delta H$: enthalpy of formation (J mol$^{-1}$)
$\dot{H}$: enthalpy flux (J s$^{-1}$)
$i$: current density (A cm$^{-2}$)
$J_k$: species flux (mol m$^{-2}$ s$^{-1}$)
$K_g$: number of gas-phase species
$n$: number of charge transferred
$Nu$: Nusselt number
$p$: pressure (Pa)
$P_e$: MEA perimeter (m)
$Pr$: Prandtl number
$Q_{ohmic}$: ohmic heat source (J m$^{-3}$ s$^{-1}$)
$R$: gas constant (J mol$^{-1}$ K$^{-1}$)
$Re$: Reynolds number
$\dot{s}$: molar production rate (mol m$^{-2}$ s$^{-1}$, mol m$^{-3}$ s$^{-1}$)
$\Delta S$: entropy change (J K$^{-1}$)
$t$: time (s)
$T$: temperature (K)
$v$: velocity (m s$^{-1}$)
$V$: volume (m$^3$)
$W_k$: molecular weight of $k$th species (kg mol$^{-1}$)
$[X]$: concentration (mol m$^{-3}$)
$x, y, z$: coordinate direction (m)
$X$: mole fraction
$Y$: mass fraction

*Greek symbols*
$\gamma$: channel density (m$^{-2}$)
$\delta$: Kronecker delta symbol
$\varepsilon$: emissivity
$\lambda$: thermal conductivity tensor (J m$^{-1}$ s$^{-1}$ K$^{-1}$)
$\mu$: viscosity (kg m$^{-1}$ s$^{-1}$)
$\rho$: density (kg m$^{-3}$)
$\sigma_e$: conductivity (S cm$^{-1}$)
$\sigma$: Stefan–Boltzmann constant (W m$^{-2}$ K$^{-4}$)
$\tau$: tortuosity
$\phi$: porosity
$\Psi$: heat flux (J m$^{-2}$ K$^{-1}$)

*Subscripts*
c: channel
e: electrolyte/electrode
f: fluid
I: interconnect
k: species index